

# Engineering Organization of DNA Nano-Chambers through Dimensionally Controlled and Multi-Sequence Encoded Differentiated Bonds

Zhiwei Lin, Hamed Emamy, Brian Minevich, Yan Xiong, Shuting Xiang, Sanat Kumar, Yonggang Ke, and Oleg Gang\*

Cite This: <https://dx.doi.org/10.1021/jacs.0c07263>

Read Online

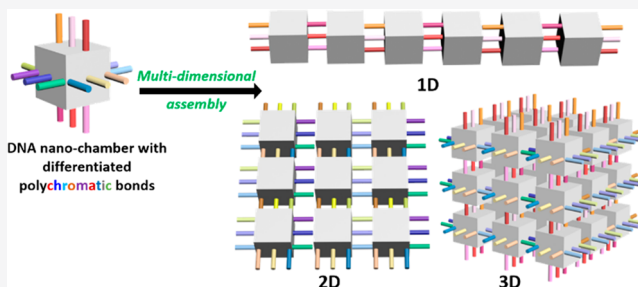
ACCESS |

Metrics & More

Article Recommendations

Supporting Information

**ABSTRACT:** Engineering the assembly of nanoscale objects into complex and prescribed structures requires control over their binding properties. Such control might benefit from a well-defined bond directionality, the ability to designate their engagements through specific encodings, and the capability to coordinate local orientations. Although much progress has been achieved in our ability to design complex nano-objects, the challenges in creating such nano-objects with fully controlled binding modes and understanding their fundamental properties are still outstanding. Here, we report a facile strategy for creating a DNA nanochamber (DNC), a hollow cuboid nano-object, whose bonds can be fully prescribed and complexly encoded along its three orthogonal axes, giving rise to addressable and differentiated bonds. The DNC can host nanoscale cargoes, which allows for the integration with functional nano-objects and their organization in larger-scale systems. We explore the relationship between the design of differentiated bonds and a formation of one-(1D), two-(2D), and three-(3D) dimensional organized arrays. Through the realization of different binding modes, we demonstrate sequence encoded nanoscale heteropolymers, helical polymers, 2D lattices, and mesoscale 3D nanostructures with internal order, and show that this assembly strategy can be applied for the organization of nanoparticles. We combine experimental investigations with computational simulation to understand the mechanism of structural formation for different types of ordered arrays, and to correlate the bonds design with assembly processes.



## INTRODUCTION

Although it is well understood that the properties of materials are determined by their primary chemical composition, coordination motifs, and large-scale organization, engineering material systems with such exquisite control represents a significant and intricate challenge.<sup>1</sup> In a myriad of examples, one-dimensional (1D), two-dimensional (2D) and three-dimensional (3D) organizations are formed from atoms and molecules, depending on their valences and anisotropic binding modes.<sup>2</sup> In particular, the well-defined valency of a carbon atom can give rise to a diversity of structures and properties, ranging from 1D carbon nanotubes to 2D graphene and 3D diamond crystals.<sup>3</sup> Much of the progress in recent years has focused on establishing methods for building nanoscale and mesoscale systems that can mimic atomic analogs<sup>4</sup> through encoding “valences” on nanoobjects and colloids.<sup>5</sup> The field has made tremendous advancements toward this goal by demonstrating and studying the objects with well-defined valences at the nanometer and micrometer length scales.<sup>6</sup>

With the ability to engineer nano-objects from the ground up, new valence modes, beyond existing atomic valences, can

be developed. These include (but are not restricted to) spatial control over interbond orientation and their specific designation. In contrast to atoms, for which valence bonds are indistinguishable from each other (Figure 1a, left), a building block with such designated bonds can support diverse binding modes. This level of control can facilitate the mutual orientation of objects into specific motifs and thus lock in the desired structural arrangement. Thus, conceptually, the ability to engineer systems with *differentiated* bonds (Figure 1a, middle) can provide opportunities for directing the organization of building blocks<sup>5b,g,7</sup> beyond those achievable at the atomic organizations<sup>4a,b</sup> and, potentially, to control the assembled structures and assembly pathways.<sup>8</sup>

Received: July 7, 2020

Published: September 9, 2020

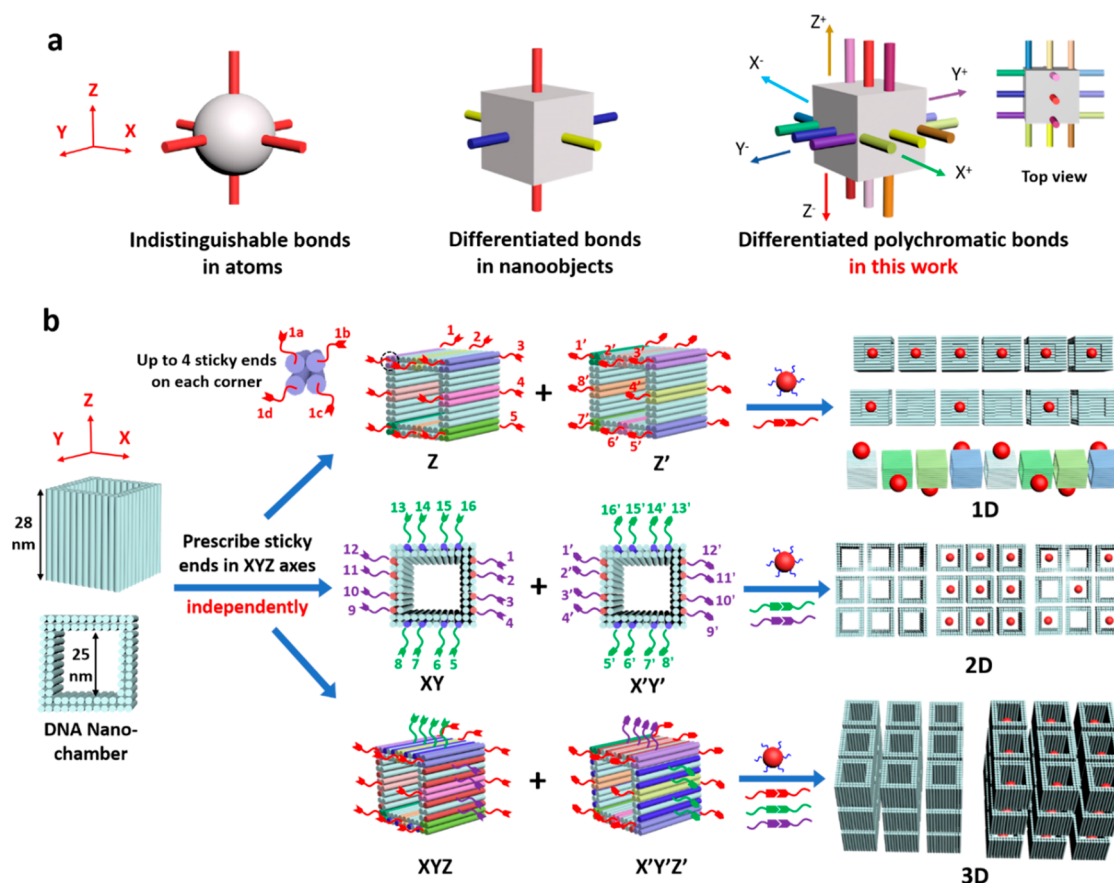


**Figure 1.** (a) Conceptual illustration of building blocks with different types of bonds. Indistinguishable bonds in atoms (left); differentiated bonds in nanoobjects (middle); and differentiated polychromatic bonds in this work (right). (b) Schematic of programmable assembly of DNA nanochambers (DNCs). Designed DNC is constructed by double layer DNA duplexes described as cylinders. Binding strands for DNC–DNC recognition along the X, Y, and Z axes can be encoded independently, which define the orthogonal distinguishable bonds of DNC. Within each axis, polychromatic bonds can be programmed and differentiated by a composition of different single-stranded DNAs (sticky ends). Colored cylinders denote the DNA duplexes designated for placing binding strands. Each binding strand consists of an 8-base sticky end and a 22-base poly-T spacer (Figure S1c). To grow 1D assemblies, complementary sticky ends are anchored to two DNCs (Z and Z') along their Z axis; on each corner, up to 4 distinct sticky ends can be accommodated. To construct 2D assemblies, complementary sticky ends are placed within the XY plane for two DNCs (XY and X'Y'). To design 3D assemblies, complementary sticky ends are installed along X, Y, and Z three axes of two DNCs (XYZ and X'Y'Z'). DNCs can be encoded with anchoring strands to capture nanoparticles in a controlled manner, giving rise to a variety of desired nanoarchitectures and periodic nanoparticles arrays.

Among the classes of assembling building blocks studied, DNA has attracted extensive interest due to its programmable sequence-specific interaction,<sup>9</sup> which allows one to prescribe different types of bonds.<sup>4a</sup> In particular, the DNA origami technique,<sup>10</sup> which involves the folding of a long DNA scaffold by hundreds of short DNA strands (“staples”), provides a powerful tool for building DNA nanoobjects with customizable architectures.<sup>11</sup> These DNA nanoobjects are of great interest for both fundamental studies and practical applications because they are capable of carrying functional guest objects such as nanoparticles,<sup>12</sup> carbon nanotubes,<sup>13</sup> enzymes,<sup>14</sup> and drugs<sup>15</sup> for customized purposes.<sup>16</sup>

The programmable nature of DNA origami building blocks make them suitable for the assembly of complex nanostructures.<sup>17</sup> Researchers revealed that DNA nano-objects can be implemented as basic building blocks for creating 1D, 2D, and 3D well-ordered nanostructures at the micrometer-scale.<sup>18</sup> Most of these formed nanostructures were constructed using a sophisticated DNA origami that was designed to support a specific binding mode, as determined by its geometry and symmetry. For example, linear DNA constructs were employed

to polymerize 1D nanostructures,<sup>19</sup> while planar DNA objects were used to yield 2D ordered arrays,<sup>20</sup> and polyhedral DNA frames of different types were designed to crystallize into 3D lattices.<sup>4c,18h,21</sup> Recent studies demonstrated that polyhedral DNA nanoobjects,<sup>4c,21a</sup> so-called material voxels, can provide different valences through their vertex-to-vertex bindings, thus, giving rise to a variety of self-assembled ordered phases while incorporating nanomaterials of different kinds, from inorganic nanoparticles to proteins and enzymes. In this approach, all bonds are equivalent and with point-like contacts between them, therefore, such systems mirror atomic systems. Alternatively, it will be advantageous to generalize the systems that can expand binding modes beyond the atomic analogs. This can be achieved by introducing bonds that can be specifically prescribed and differentiated in space to support the engineered assembly of arbitrary architectures. From the nanomaterial fabrication perspective, it is important that such capabilities for the design of binding modes could allow for the integration of organic and inorganic functional nano-objects. On a fundamental level, it is also critical to understand the self-assembly pathway for the systems with designed bonds,

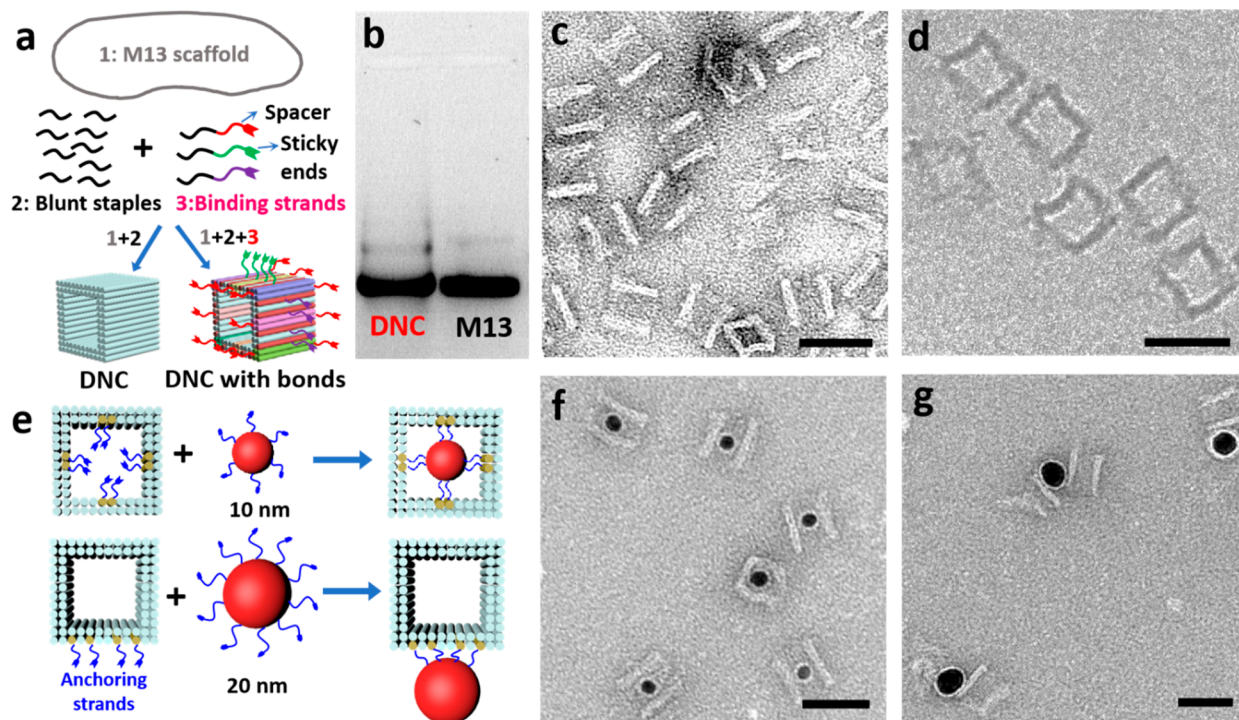


**Figure 2.** Construction of DNA nanochambers and their ability to carry AuNPs. (a) Formation of DNC by folding an M13 scaffold with 224 blunt staples. To fabricate DNC for subsequent assembly, interchamber binding strands with sticky end sequences are introduced during the origami folding process. (b) Agarose gel electrophoresis analysis of DNCs. (c) Negatively stained TEM image of DNCs. (d) Cryo-TEM image of DNCs. (e) Schematic illustration of encapsulating AuNPs in the cavity or on the sidewall of DNCs by anchoring strands. TEM images of DNCs bound with (f) 10 nm AuNP in the cavity, and (g) 20 nm AuNP on the bundle of one sidewall. Scale bar: 50 nm.

associated kinetic effects, and the relationship between the system design and the formed structures.

In this study, we investigate a nanoscale system that satisfies these requirements and possesses the following features (Figure 1a, right): (i) a rigid 3D semiclosed cuboid geometry that can carry nanocargo; (ii) differentiated bonds, through DNA-encoding, for prescribing interobject connectivity in three orthogonal directions and their local alignments; (iii) multisequence encoding of bonds (polychromatic bonds) within each axis that have a robust prescription of interactions along with control over a relative orientation of objects. Here, as the fundamental building block, we use a DNA nanochamber (DNC), a hollow DNA cuboid. Such an object has an intrinsically relatively low symmetry, which well supports the designability of complex architectures, has well-defined internal arrangement of duplexes, and possesses an internal compartment that allows it to host a nanoparticle or a molecule or a biomolecular complex. Two openings of the DNC also permit the ease of inserting and release of nanocargo. Thus, the DNC combines a simple yet relevant geometrical shape with a potential utility for exploring assembly using differentiated bonds. Our study shows a facile approach to regulate the programmable assembly of these blocks into multidimensional ordered arrays with different degrees of complexity through control of differentiated polychromatic bonds (Figure 1b). Using electron microscopy and in situ X-ray scattering methods we reveal that engaging bonds along one (*Z*), two (*X,Y*) and three (*X, Y, Z*) axes results in the formation of 1D, 2D, and 3D ordered arrays, respectively, while the strength of the bonds and their differences have effect on the assembled structures. We further show that the resultant arrays can serve as versatile platforms to coordinate the organization of gold

nanoparticles (AuNPs). Combining with computer simulations, we uncover the contribution of bond dimensionality and their designs on structure formation, as well as elucidate the observed self-assembled morphologies.

## RESULTS AND DISCUSSION

**Design of DNA Nanochamber and Establishment of Differentiated Polychromatic Bonds.** In this work, we propose and realize building blocks (DNCs) with bonds that are fully differentiated in the *X*, *Y*, and *Z* directions and within each axis (Figure 1a). Thus, DNC binding properties are determined by 6 unique types of bonds:  $X^-$ ,  $X^+$ ,  $Y^-$ ,  $Y^+$ ,  $Z^-$ , and  $Z^+$ . We will typically refer to them simply as *X*, *Y*, and *Z* bonds. Moreover, in our approach we encode each bond via multisequence strands, so-called “sticky ends”, that offer a high degree of uniqueness for encoding, orthogonality of interactions, orientation, and positioning control. Since each sticky end is encoded with a distinct DNA sequence, we thus refer as to it as “color”, and this differentiation allow us to establish polychromatic *X*, *Y*, and *Z* bonds. The bonds are located at the well-defined positions along the surface of the DNC. The assembly of DNC monomers into a larger-scale organization is dictated by these polychromatic bonds, while the specific details of bonds can influence the assembly process, as revealed by our study. This strategy offers designability of anisotropic and differentiated bonds for engineering ordered arrays using the same basis nanoobject, the DNA nanochamber.

In our experimental design, DNC consisting of a total of 80 DNA duplex cylinders was designed by caDNAo (see Figures S1 and S2 of the Supporting Information, SI, for design in details). The DNC has an open cavity of size  $\sim 25 \times 25 \times 28$

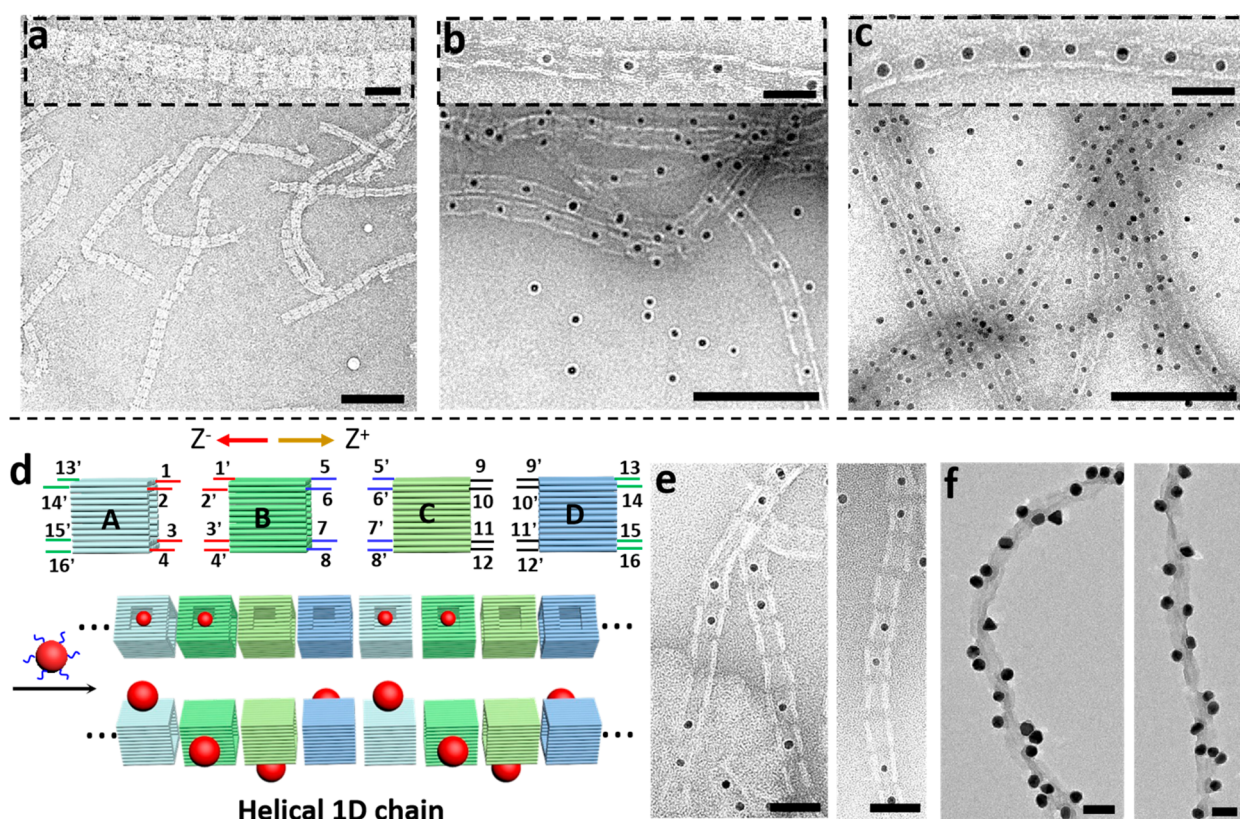


**Figure 3.** 1D assembly of DNA nanoarchitectures. TEM images of (a) empty 1D chains, (b) 1D alternating chains alternatively filled with 10 nm AuNPs, and (c) 1D homochains fully filled with 10 nm AuNPs. Insets are zoomed-in views of the respective structures. These 1D chains were polymerized from a design incorporating 32 sticky ends. (d) Schematic illustration for creating 1D polymer chain with controlled monomer sequence of ABCD, where A, B, C, and D are four different kinds of DNCs, specifically designed in a way that their complementary sticky ends promote a connectivity of a defined sequence of DNCs. For simplicity, only 4 out of 32 sticky ends are showcased on each side of DNCs. The numbers indicate distinct DNA sequences of all sticky ends, which determine the definitive ABCD connecting sequence and orientation of four monomers. (e) TEM images of linear 1D chains consisting of two 10 nm AuNPs-filled and two empty DNCs in an alternating manner. (f) TEM image of helical 1D chains bound 20 nm AuNPs on the sidewall of DNCs in a helical architecture. Scale bars: 200 nm for (a–c), 50 nm for insets, and 50 nm for (e) and (f).

$\text{nm}^3$ , which is fenced by a double layer of DNA duplexes. As highlighted by colored duplexes, binding strands for inter-chamber connections can be independently tuned and are located in the middle of the DNC walls for XY directions, and at the edges of the DNC opening for Z direction. Each binding strand consists of an 8-base recognition sequence (sticky ends) and a 22-base poly-T DNA spacer. The poly-T spacers endow the flexibility of linkages and mediate steric effects, both of which are beneficial for DNC–DNC recognition during assembly. In addition to differentiated bonds along orthogonal  $X^-$ ,  $X^+$ ,  $Y^-$ ,  $Y^+$ ,  $Z^-$ , and  $Z^+$  axes, all of 8-base sticky ends within each axis are entirely distinct as denoted by different numbers (e. g., 1–16 in XY). Again, we refer to these distinct sticky ends along each axis as having a different color and therefore call them polychromatic bonds. Not only do these polychromatic bonds enable the connected DNCs to align correctly and prevent uncontrolled shifting, but, more importantly, they also endow orientational control of monomers within ordered arrays. These design principles of programmable polychromatic bonds are applied to 1D, 2D, and 3D assemblies.

**DNA Nano-chamber Construction and Nanoparticles Encapsulation.** DNC was formed by folding an M13mp18 single-stranded (ss) scaffold with 224 short staple oligonucleotides (Figure 2a), through slowly cooling from 80 °C to room temperature (see SI for details). The successful formation of

DNC was first analyzed by agarose gel electrophoresis (Figure 2b). The gel-purified products were then examined by negative-staining transmission electron microscopy (TEM). Hollow DNA frames with a height of 28 nm were observed (Figures 2c and S3), which unambiguously confirmed the formation of the designed construct. Cryo-TEM was utilized to further verify the DNC structure. As shown in Figure 2d, hollow cuboid architectures with a central cavity of 25 nm and wall thickness of ~5 nm can be visualized directly, in good agreement with double layer packing of DNA helix. The binding strands for interchamber ligation can be readily incorporated through introducing selected staple strands containing extension sequences of sticky ends during the DNA origami folding protocol (see DNC with bonds in Figure 2a).

DNCs can be encoded with internal and external anchoring strands for carrying nanocargo, in this case AuNPs, within the cavity or outside of the sidewall (Figure 2e), respectively. The integration of DNCs and AuNPs was achieved by annealing the DNCs encoded with anchoring strands and AuNPs functionalized with complementary ssDNA strands. The AuNPs and DNCs (typically, 60  $\mu\text{L}$  of 10 nM) were mixed in a stoichiometric ratio of 2.5:1, and subjected to an overnight annealing procedure. As illustrative examples, AuNPs with core diameters of 10 nm (18-base DNA shell) and 20 nm (18-base

DNA shell) were employed to coordinate with the DNCs, respectively. TEM imaging after gel purification confirms a successful encapsulation of 10 nm AuNPs in the DNCs with a yield of 93% (Figures 2f and S4), and a binding of 20 nm AuNPs onto the sidewall with a yield of 81% (Figures 2g and S4). It is worth noting that each cavity (25 nm) and sidewall (28 nm) can accommodate only one DNA-coated AuNP, which is essential for controlling the arrangement of AuNPs within ordered arrays as we discuss below.

**1D Assembly of DNA Nanochambers.** By utilizing DNCs with fully prescribed binding characteristics as underlying building blocks, we first demonstrate the assembly of 1D linear arrays, which represent a nanoscale polymer analog.<sup>22</sup> The use of differentiated bonds and type-encoded DNCs allows us to construct a variety of nanoparticle architectures, as we show below, including homopolymers, sequence-prescribed heteropolymers, and helical polymers. To assemble the chain-like 1D arrays, sticky ends are placed as extensions of selected staples at the end of the DNA duplex along the Z-axis. Two types of DNCs (e.g., Z and Z') containing sticky ends complementary to each other were designed, giving rise to two kinds of bifunctional "monomers".<sup>22</sup> For each monomer, we can attach up to 32 binding strands at the predefined locations of DNC edges (Figure 1b), where their 8-base sticky end sequences are completely different from each other. This multisequence encoding along the Z-axis allows for a high degree of specificity of DNC–DNC bindings and for controlling their relative orientation along Z direction. We selected 8-base sticky ends because their melting temperatures are within a favorable experimental annealing temperature window (20–50 °C). We also tested 6-base or 10-base sticky ends using identical annealing protocol. We observed unconnected or aggregated structures (see Figure S5 and additional discussion), respectively. Therefore, we used 8-base sticky ends design for all systems discussed in this work. Analogous to classic step-growth polymerization, the ligation of DNCs was induced by slowly cooling mixtures containing equal amount of two monomers (typically, 100  $\mu$ L of 10 nM). To enable a proper antiparallel directionality for the hybridization of sticky ends, Z' monomer is specifically designed to rotate 90° clockwise relative to Z monomer in the direction of polymerization (see the design details in Figure S6).

The discussed DNC system with Z bonds has a similarity with a classic step-growth polymerization, for which the prerequisite of synthesizing long polymer chains is highly reactive monomers. In order to identify the high "reactivity" for 1D growth in our case, we explored the chain formation by varying the number of sticky ends on each side of DNC (from 8, 16, 24 to 32). When 8 sticky ends were used, oligomers with an average of 4 monomers long were observed (Figure S7). Increasing the number of sticky ends to 16, both oligomers and polymers were yielded with an average of 8 monomers per chain (Figure S8). Further increase of sticky end number (24 and 32) results in longer nanopolymer chains (Figures S9 and S10). Notably, using 32 sticky ends, we obtained discrete chains with micrometer lengths containing on average 30 monomers (Figures 3a and S10). We stress that formation of chains requires an annealing process, without which disordered aggregates are observed. Annealing involves a slow cooling of the sample from 50 to 20 °C (see SI for details). During this process there is a temperature window within which quasi-equilibrium assembly occurs with reversible bindings of individual sticky ends. For an assembly regime within this

favorable temperature window (FTW), the growth rate depends on the inter-DNC interaction strength and binding probabilities, which for the given sticky end motifs are determined by the number of sticky ends. Since all systems follow the same annealing protocol, they spend the same amount of time in the FTW. This results in the assembly of longest chains for the 32 sticky ends design, which has the largest attraction interaction among the discussed systems (Figures S7–S10).

On the basis of the design of 32 sticky ends, we fabricated different types of linear AuNPs chains via a "one-pot" assembly process, where DNA-coated AuNPs, Z, and Z' DNCs encoded with internal anchoring strands were simply mixed and annealed to grow 1D nanoparticles arrays in one step. We term the process a "one-pot" here because AuNPs loading and DNC polymerization occur concurrently in one annealing protocol. To ensure satisfactory loading efficiency of AuNPs, we implemented (i) stronger bonds, based on 12-base internal anchoring strands, for AuNPs encapsulation, in comparison with 8-base sticky ends for polymerization, and (ii) the excess of AuNPs (molar ratio AuNPs/DNC = 2/1). This one-pot approach is also applied to the 2D and 3D assembly (see below). The alternating/homo-chains that are alternatively/fully filled with 10 nm AuNPs were produced by encoding single (Z or Z')/both (Z and Z') DNC monomers with internal anchoring strands. The desired nanostructures were directly visualized from TEM images in Figure 3b,c, with a success rate of 83% and 89% for filling alternating chains and homochains with AuNPs, respectively (additional images can be seen in Figure S11).

Given a full prescription of bonds and DNCs encoding for both external and internal connection, the presented approach for constructing polymer-like chains is both robust and versatile. In principle, it can be adapted to build chains with increasing complexity and arbitrary order of different monomers. To demonstrate this versatility, four different kinds of DNCs were specifically designed (e.g., A, B, C, and D), whose complementary sticky ends allow for connecting with each other sequentially (Figure 3d). Upon annealing in a rigorous equal molar ratio, the desired nanoscale heteropolymer with a definitive sequence of ABCD was produced (Figure S12a). Notably, the sequence-controlled chains offer a platform for controlled nanoparticle arrangement in a complex linear array. For example, we built a new alternating nanoarchitecture in which two filled and two empty DNCs are alternatively arranged (Figure 3e). Within this nanoarchitecture, monomers A and B are designed with internal anchoring strands to capture 10 nm AuNPs, while monomers C and D do not have these strands.

To stress the significance of monomer orientation control through multisequence bonds, we further created a helical organization within the 1D array by placing 20 nm AuNPs on the specifically designated sidewall of four types (A, B, C, and D) of DNCs (see Figure S12b for detailed design). This assembly requires the specific orientation of monomers relative to their adjacent neighbors, and the discussed multisequence scheme permits for such a realization (Figure 3d). The defined 1D arrays with helical nanoparticle organization were successfully fabricated and verified by TEM imaging (Figure 3f). While other studies used a single DNA origami construct as a template for the fabrication of AuNPs helices,<sup>23</sup> the approach demonstrated here is conceptually different since the helical organization is derived from the assembly of multiple

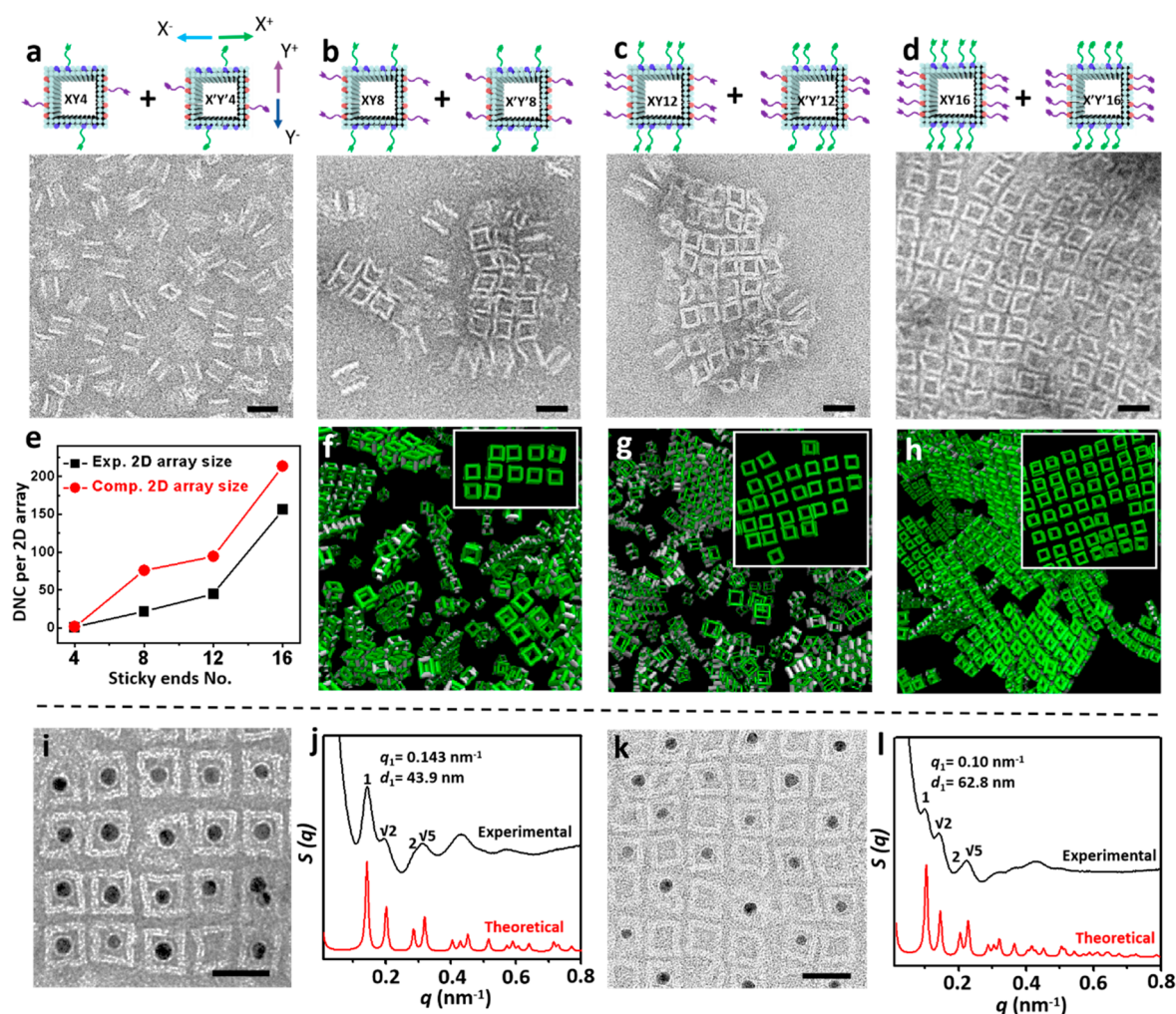


**Figure 4.** 2D assembly of DNA nanochambers. (a–d) Schematic illustration and TEM images of 2D arrays assembled from two complementary DNCs with varying number of sticky ends within the XY-plane. (a) 4 sticky ends, (b) 8 sticky ends, (c) 12 sticky ends, and (d) 16 sticky ends. (e) Statistical analysis of average 2D array size with increasing sticky ends, based on both experimental results (black square) and computational simulation (red circle). (f–h) Monte Carlo simulation snapshots of 2D arrays created by variation of binding strength. (f) 8 bonds, (g) 12 bonds, and (h) 16 bonds. Insets are representative individual 2D arrays. (i) TEM image and (j) SAXS pattern of 2D square lattices fully filled with 10 nm AuNPs. (k) TEM image and (l) SAXS pattern of chess-board-like 2D lattices alternatively filled with 10 nm AuNPs. Both 2D AuNP lattices utilize the design with 16 sticky ends per DNC. Scale bar: 50 nm.

types of DNC monomers. As each monomer can be independently programmed, this may provide new opportunities to tailor chiral organizations in terms of their length, composition, and architecture, and potentially allow for dynamic regulation of the formed structures.

**2D Assembly of DNA Nanochambers.** Four-fold symmetry of DNC in the lateral direction (XY, Figure 1b) permits for the manipulation of 2D square arrays by encoding bonds on four sidewalls of adjacent, complementary DNCs (e.g., XY and X'Y'). Up to four distinct sticky ends with a defined order were used to prescribe a recognition zone on each DNC face along the center-line in the XY plane of each sidewall (see Figure S13 for detailed design). This encoding provides positioning restrictions ensuring the ligation of two neighboring DNCs in the same plane, whereas the implementation of distinct sequences for face-to-face bonds prevents any undesired lateral shifting.

To induce 2D array formation, equal amounts of two complementary DNC mixtures were subjected to a 48 h annealing process (cooling from 50 to 20 °C). Figures 4a–d

and S14–S17 demonstrate the successful assembly of 2D arrays for different number of sticky ends in the XY-plane (total per DNC: 4, 8, 12, and 16, or per DNC's face: 1, 2, 3, and 4). For 4 sticky ends, the binding strength is too weak to bridge neighboring DNCs (Figure 4a). As we increase the number of sticky ends from 8 to 12, and finally to 16, the average domain size of 2D arrays increases dramatically from 22 to 45 to 156 DNCs per array (Figure 4b–e), respectively. We attribute this positive correlation between the number of sticky ends and the size of the 2D array to the increased inter-DNC hybridization energy and binding probability. We note that the process of lattice formation occurs during annealing in the FTW, similar to the 1D case. The same mechanism (as discussed for 1D case) is realized for 2D system: the growth rate within FTW influences the size of the crystalline domain, and that rate is higher for the larger number of the sticky ends. With 16 sticky ends, we observed the formation of the prescribed large-domains of DNC 2D lattice (Figures 4d and S17). Small angle X-ray scattering (SAXS) characterization reveals a typical scattering profile for 2D square lattices (Figure

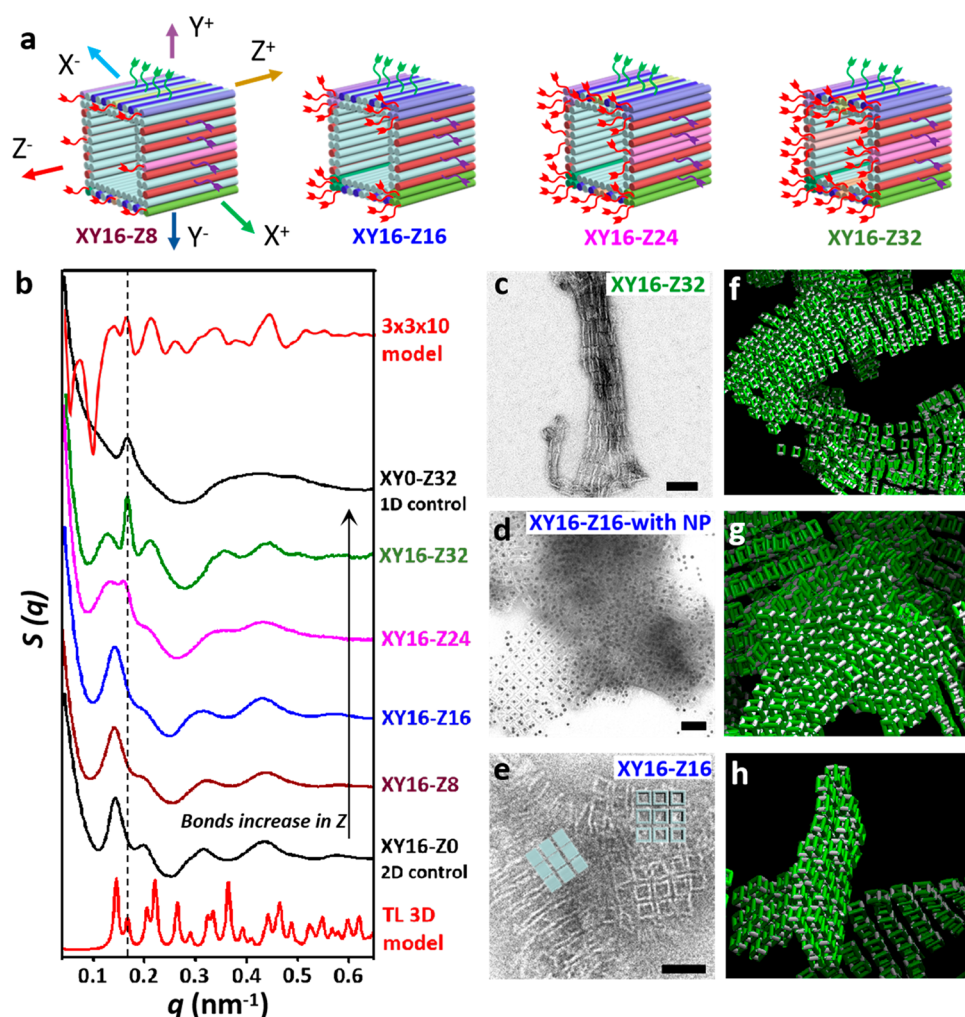


**Figure 5.** 3D assembly of DNA nanochambers. (a) Illustration of four types of DNCs with different binding modes, denoted as  $XY_m-Z_n$ , which are designed for 3D assembly.  $XY_m-Z_n$  DNCs contain  $m = 16$  sticky ends within the lateral  $XY$ -plane and varying numbers ( $n = 8, 16, 24,$  and  $32$ ) of sticky ends in the longitudinal  $Z$  direction. For simplicity, only half of sticky ends are shown for a DNC. (b) Structure factor,  $S(q)$ , for assembly of  $XY_m-Z_n$  DNCs filled with AuNPs for different designs in panel a.  $S(q)$  of  $XY_0-Z_{32}$  forming 1D array,  $XY_{16}-Z_0$  forming 2D array, modeled  $S(q)$  of the tetragonal lattice (TL) and the mesoscale finite 3D tetragonal DNC array ( $3 \times 3 \times 10$ ) with encapsulated AuNPs. (c) TEM image of elongated 3D structures formed by empty  $XY_{16}-Z_{32}$  DNCs. (d, e) TEM images of (d) AuNPs-filled and (e) empty 3D assembly for  $XY_{16}-Z_{16}$  DNCs. In panel e, two scenarios viewed from parallel with and perpendicular to  $Z$ -axis can be observed. (f–h) Monte Carlo simulation snapshots of various 3D assembled structures created by variation of relative binding energies in  $XY$ -plane versus  $Z$ -axis. (f) fiber-like ( $Z$ -dominant) domains of 3D assembled DNCs with strong longitudinal bonds; (g) cubic-like domains of 3D assembled DNCs with balanced longitudinal and lateral bonds; and (h) pancake-like ( $XY$ -dominant) domains of 3D assembled DNCs with strong lateral bonds. Scale bar: 100 nm for (c–e).

S18). The scattering peaks corresponding to Bragg reflection planes: (10) (11) (20) (21) (30) (31) and their positions agree well with the modeled scattering. The center-to-center distance of two adjacent DNCs is 44.2 nm based on the first order peak (10) and is consistent with that measured from TEM observations. These results validate that the formation of 2D ordered arrangements of DNCs within the  $XY$ -plane occurs in the bulk.

To further understand the experimental results on assembly of the 2D DNC arrays, we performed molecular dynamics simulations. We used a cubic hard object as a proxy for the designed DNC and the Kern-Frenkel potential to mimic inter-DNC bonds. In order to reflect the specificity of bonds in the experimental system, we designed different types (“colors”) of bonds for each sticky end strand on the cube, wherein only the same color of bonds can bind to each other (more details regarding the simulations can be found in SI). Using Monte Carlo simulation of hard polyhedral (HOOMD-blue pack-

age),<sup>24</sup> we cooled the systems with 4, 8, 12, and 16 bonds down from high temperature and calculated the average assembled cluster sizes (Figure 4e–h). Similar to the experimental findings, the average cluster size becomes larger as the number of bonds increase from 4 to 16. This effect is due to a higher growth rate of ordered domains for a larger number of sticky ends. The simulation indicates that the crystallization rate can significantly affect the final size of the clusters (Figure S30), and the binding probability enhances as the number of bonds increases (Figure S31), leading to larger sizes of clusters within the same simulation time scale.

Next, we used DNCs that were encoded with internal anchoring strands to form 2D lattices of AuNPs. With the design of 16 bonds per DNC, 2D lattices of AuNPs were produced via a one-pot protocol where we annealed AuNPs with DNCs (molar ratio: AuNPs/DNC = 2/1). TEM observation and well-defined SAXS pattern validate the formation of the intended 2D AuNP lattices (Figures 4i,j

and S19). It should be noted that compared with the SAXS pattern of vacant DNC arrays (Figure S18), the SAXS scattering profile in Figure 4j is much sharper and fully reflecting the AuNPs arrangement due to high X-ray contrast of AuNPs relative to DNA. The normalized peak positions in the SAXS pattern show a  $q_n/q_1$  ratio of 1:  $\sqrt{2}$ :2:  $\sqrt{5}$ . . . ( $q_1 = 0.143 \text{ nm}^{-1}$ ), unambiguously identifying a conventional 2D-square lattice. The close correspondence with the model peak positions (red line in Figure 4j) indicates a formation of well-defined square lattice. Moreover, the center-to-center distance of two neighboring AuNPs obtained from SAXS ( $d_1 = 43.9 \text{ nm}$ ) is in good agreement with that from TEM image ( $\sim 44 \text{ nm}$ ), further suggesting a high degree of order for assembled AuNP lattices. To emphasize the versatility of this approach for engineering particle arrangements, we further designed a chess-board-like 2D lattice with alternative loading of AuNP in DNCs (Figure 4k). The chess-board-like 2D lattices were also characterized by SAXS, where the experimental scattering peaks are consistent with the model (Figure 4l). The resulting lattice with well-defined order has a  $\sqrt{2}$ -fold increase in the center-to-center nanoparticle distance ( $d_1 = 62.8 \text{ nm}$ ) in comparison with the previous design for a flat square lattice shown in Figure 4j (see additional analysis in Figure S20).

**3D Assembly of DNA Nanochambers.** We further extend the presented strategy to create DNCs with differentiated bonds in all three orthogonal directions and to explore their assembly behaviors. The complementary sticky ends were anchored along the three axes of DNC to construct the 3D assembly, essentially combining approaches for the formation of the aforementioned 1D and 2D arrays. This seemingly simple addition of Z and XY interactions induces a quite nontrivial assembly behavior in 3D due to the competition between these longitudinal (Z) and lateral (XY) binding modes. Indeed, the reported computational studies demonstrated the sensitivity of 3D ordered assembly to the details of bonds design.<sup>25</sup> Compared with 1D or 2D arrays, the growth of 3D structures within the XY-plane versus along the Z-axis resembles a tug-of-war, and this interplay has significant impacts on the assembly kinetics and ultimately the structures formed. In an effort to control the assembly process for DNCs with XYZ bonds, we used the 3D design with 16 sticky ends within the XY-plane that has previously been proved to afford well-defined 2D arrays, and varied the number of sticky ends along the Z-axis from 8, 16, 24, to 32 (Figure 5a). For simplicity, we refer to them as  $XY_m-Z_n$ , where  $m$  and  $n$  denote the number of sticky ends prescribed in the XY-plane and along the Z-axis, respectively. Note that sequences of these ( $m + n$ ) sticky ends attached to a single DNC are entirely distinct from each other, and bonds for each axis (X, Y, and Z) are differentiated from each other.

Following 3D assembly of these DNCs, we performed SAXS measurements to explore the structures of the resultant assemblies. Figure 5b illustrates both experimental and modeled SAXS patterns of assembled structures for the relevant designs ( $m = 16$  and  $n = 8, 16, 24-32$ ). To enhance the X-ray scattering signal, the DNCs for all designs were filled with 10 nm AuNPs. Two additional experimental scattering patterns are shown as controls for the 3D assembly. The first control is the  $XY_0-Z_{32}$  (interparticle distance  $c = 37.8 \text{ nm}$ ) that assembles into 1D chains, due to the absence of a lateral binding mode, and the other one is the  $XY_{16}-Z_0$  (lattice constant  $a = b = 43.9 \text{ nm}$ ) that assembles into 2D arrays (adapted from Figure 4j), due to the absence of the

longitudinal binding mode. On the basis of the symmetry of DNC and these controls, one could expect that assembled 3D DNC arrays should correspond to that of a lattice with a primitive tetragonal unit cell whose lattice parameters are  $a = b = 43.9 \text{ nm}$ ,  $c = 37.8 \text{ nm}$ ,  $\alpha = \beta = \gamma = 90^\circ$ . A modeled scattering pattern for this tetragonal lattice (TL) was thus generated and is displayed on the same plot. However, the comparison of the generated scattering pattern of a tetragonal lattice to the experimentally obtained patterns for the  $XY_{16}-Z_8$  and  $XY_{16}-Z_{16}$  systems reveal significant differences. The structure factors ( $S(q)$ ) of  $XY_{16}-Z_8$  and  $XY_{16}-Z_{16}$  instead resemble that of  $XY_{16}-Z_0$  (2D arrays), implying that the lateral growth dominates the assembly process. We note that similar to 1D and 2D systems, discussed above, the growth of 3D system within FTW of annealing might depend on the relative interaction strength of XYZ bonds. In general, this might result in the anisotropic growth or limited growth along the XY and Z direction. We hypothesize that since the growth rate in the XY and Z direction might be different for bond designs, the assembled structure is likely to be anisotropic, reflecting differences in growth rates. To further elucidate the structure of the assemblies we have conducted detailed electron microscopy study.

We show in Figure 5d,e the TEM images of  $XY_{16}-Z_{16}$  with and without encaging AuNPs, respectively. Large domains consisting of 2D AuNP lattices can be clearly visualized in Figure 5d. Considering the 2D projection feature of TEM imaging, it is challenging to directly identify 3D architectures from TEM observation. However, we were able to capture two different kinds of DNC packing patterns within a single domain, which are parallel alignment of short 1D chains along the Z-axis and a 2D array pattern within the XY-plane (Figure 5e), respectively. These two observed scenarios result from two projection views that are perpendicular to and parallel with Z direction of the 3D structures (see insets in Figure 5e). Taken together, these results support our suggestion that the growth of structures dominate within the XY-plane, leading to the formation of 3D structures with a limited number of layers along the Z-axis for  $XY_{16}-Z_8$  and  $XY_{16}-Z_{16}$ .

We note that the scattering profiles clearly evolve with increasing bond strength (the number of sticky ends) along the Z-axis. For  $XY_{16}-Z_{24}$  and  $XY_{16}-Z_{32}$ , the structure factors exhibit significant deviation from that of the 2D control ( $XY_{16}-Z_0$ ), but these patterns still do not resemble that of the expected tetragonal lattice. In the case of a strong longitudinal binding mode,  $XY_{16}-Z_{32}$ , the scattering profile exhibits a peak at  $q = 0.166 \text{ nm}^{-1}$  (guided by the dash line) that corresponds to the center-to-center distance of two adjacent DNCs in 1D chains, as seen in the SAXS data of the 1D control sample ( $XY_0-Z_{32}$ ). Note that this peak is not present in  $XY_{16}-Z_8$  and  $XY_{16}-Z_{16}$  scattering patterns. This suggests that the packing of DNCs along the Z-axis becomes a key structural feature of this system. Such a feature is directly confirmed by TEM imaging of  $XY_{16}-Z_{32}$  (Figure 5c) in which a high aspect ratio bundle of DNCs is observed.

To further analyze the above observation for the  $XY_{16}-Z_{32}$  system, we expanded SAXS analysis toward understanding both an internal order of assembly and the morphology of assembled structure. Specifically, we modeled a finite 3D array containing 3 (X)  $\times$  3 (Y)  $\times$  10 (Z) AuNPs-filled DNCs within which DNCs are arranged in a tetragonal unit cell (see SI), as an example of a Z-elongated assembled structure. This finite model captures the feature of fiber-like 3D structures, as

observed in Figure 5c. The scattering profile of this  $3 \times 3 \times 10$  model demonstrates an excellent match with the structure factor of the XY16–Z32 system (see modeling details in SI), which further verify the feature of stacking along the Z-axis. We stress that this scattering model does not uniquely identify that the structure formed should be  $3 \times 3 \times 10$ , but it rather indicates that the 3D assemblies formed have tetragonal internal organization and a high aspect ratio, which signifies a different growth rate along the XY and Z directions. Taken together, we conclude that the XY16–Z8 and XY16–Z16 systems exhibit 2D-dominated morphology due to the relatively weak longitudinal binding. In contrast, for XY16–Z24 and XY16–Z32 systems with a strong longitudinal binding, a growth of 3D structure along Z-axis becomes dominant, leading to the formation of 3D structures with aspect ratio emphasized in the Z-direction. Within these both layer-like and fiber-like mesoscale 3D assemblies, a tetragonal organization of DNCs is still maintained due to their well-defined structure and prescribed binding modes.

To understand the effects of relative binding energies along the Z-axis versus in the XY-plane on the crystallization process, we performed molecular simulations of assembled 3D structures. The design principles and multisequence features of the bonds are similar to the 2D case, but we added one bond on each corner of the cube along the Z-axis (Figure S28). We performed the simulations by keeping the number of bonds constant (16) in the XY-plane, and the binding energy of each bond fixed ( $\frac{\epsilon}{k_B T} = 3.0$ ). We varied the binding energy of each bond in Z direction ( $3.0 < \frac{\epsilon_z}{k_B T} < 5.0$ ). We observed that the shape of clusters changes from the pancake-like 2D-dominated structures for  $\frac{\epsilon_z}{k_B T} = 3.0$  (Figure 5h), to cubic-like structures for  $\frac{\epsilon_z}{k_B T} = 4.0$  (Figure 5g), and fiber-like 1D-dominated structures for  $\frac{\epsilon_z}{k_B T} = 5.0$  (Figure 5f). We used the relative shape anisotropy ( $\kappa^2 = \frac{\frac{3}{2}(\lambda_1^4 + \lambda_2^4 + \lambda_3^4)}{(\lambda_1^2 + \lambda_2^2 + \lambda_3^2)^2} - \frac{1}{2}$ ) to quantify the shape of these resultant crystallites, where  $\lambda_i^2$  are the eigenvalues of the gyration tensor of the clusters. We calculated the  $\kappa^2$  for the largest clusters in the system, and obtained  $\kappa^2 = 0.24, 0.06,$  and  $0.75,$  for pancake-like, cubic-like, and fiber-like crystallites, respectively. These values correspond to ideal disk-like ( $\kappa^2 = 0.25$ ), cubic-like ( $\kappa^2 = 0$ ), and rod-like ( $\kappa^2 = 1$ ) geometry, respectively, which further confirm the formation of 2D-dominated, cubic, and 1D-dominated crystallites in our molecular simulation study.

Strikingly, the 2D-layer dominated (Figure 5h) and 1D-fiber dominated 3D structures (Figure 5f) predicted by simulation are qualitatively consistent with our experimental observations. However, we note that simulations predict the formation of assemblies with cubic morphology (Figure 5g), while we did not experimentally observe them. We attribute this to their narrow existence range and the details of bonds arrangements. Indeed, from the simulation results we know that the cubic-like morphologies can only occur in a very limited range of relative binding energy ( $\epsilon_z/\epsilon_{xy}$ ) along the Z-axis versus in the XY-plane. In simulation, we are able to systematically tune the value of  $\epsilon_z/\epsilon_{xy}$  to catch a cubic 3D lattice. In contrast, the changes of  $\epsilon_z/\epsilon_{xy}$  are discrete in the experimental design. As illustrated in Figure 5a, the binding energy along the Z-axis changes in a step of 8 bonds (8, 16, 24, and 32). Therefore, it is plausible that the experimental values of  $\epsilon_z/\epsilon_{xy}$  are not balanced to the

precise degree that allows for the formation of cubic-like assemblies. In addition, a location of sticky ends for the XY (along the center of face) and Z (at edges) bonds can also play a significant role due to the entropic effects and connectivity properties of individual sticky ends. Future studies will elaborate the morphological details of the 3D assemblies.

## CONCLUSIONS

In summary, we have developed a versatile strategy for creating nanoscale objects, DNA nanochambers (DNCs), with differentiated and dimensionally controlled bonds. Such objects offer polychromatic bonds, where each bond provides individual encoding with orientation and position control of inter-DNC binding, and the ability to carry nanocargoes. The ability to prescribe binding modes allows for the programmable assembly of DNCs into 1D, 2D, and 3D arrays. These structural variations are rationally achieved through fully prescribed bonds encoded along the X, Y, and Z orthogonal axes of DNCs. Our study explores the engineering of different architectures using this novel object. Specifically, we demonstrate: (i) Z encoded DNCs create homopolymers and heteropolymers with ability to control the sequences of monomers and relative orientation, thus, generating helical polymers; (ii) XY encoded DNCs form 2D ordered square arrays with regulated chamber-filling patterns wherein the sizes of the 2D ordered arrays depend on the bonds strength; and (iii) three axes encoded DNCs assemble into mesoscale-sized 3D tetragonal arrays whose morphology is a result of competing Z- and XY-bonds. Both experimental and computational studies reveal that the design of binding modes is a crucial factor in the formation of the desired structures. These results provide a new insight into the governing principles of programmable assembly and offer a versatile approach, using bond encoding, for building complex organizations from functional nano-objects that can be readily integrated with nanochambers.

## ASSOCIATED CONTENT

### Supporting Information

The Supporting Information is available free of charge at <https://pubs.acs.org/doi/10.1021/jacs.0c07263>.

Design and fabrication of DNA nanochamber, detailed experiment, modeling, and simulation description; and additional results and discussion (PDF)

## AUTHOR INFORMATION

### Corresponding Author

Oleg Gang – Department of Chemical Engineering and Department of Applied Physics and Applied Mathematics, Columbia University, New York, New York 10027, United States; Center for Functional Nanomaterials, Brookhaven National Laboratory, Upton, New York 11973, United States; [orcid.org/0000-0001-5534-3121](https://orcid.org/0000-0001-5534-3121); Email: [og2226@columbia.edu](mailto:og2226@columbia.edu)

### Authors

Zhiwei Lin – Department of Chemical Engineering, Columbia University, New York, New York 10027, United States; [orcid.org/0000-0001-9194-1145](https://orcid.org/0000-0001-9194-1145)  
Hamed Emamy – Department of Chemical Engineering, Columbia University, New York, New York 10027, United States; [orcid.org/0000-0002-5078-5569](https://orcid.org/0000-0002-5078-5569)

**Brian Minevich** – Department of Chemical Engineering, Columbia University, New York, New York 10027, United States

**Yan Xiong** – Department of Chemical Engineering, Columbia University, New York, New York 10027, United States

**Shuting Xiang** – Department of Chemical Engineering, Columbia University, New York, New York 10027, United States

**Sanat Kumar** – Department of Chemical Engineering, Columbia University, New York, New York 10027, United States; [orcid.org/0000-0002-6690-2221](https://orcid.org/0000-0002-6690-2221)

**Yonggang Ke** – Wallace H. Coulter Department of Biomedical Engineering, Georgia Institute of Technology and Emory University, Atlanta, Georgia 30322, United States; [orcid.org/0000-0003-1673-2153](https://orcid.org/0000-0003-1673-2153)

Complete contact information is available at: <https://pubs.acs.org/10.1021/jacs.0c07263>

## Notes

The authors declare no competing financial interest.

## ACKNOWLEDGMENTS

This research was supported by the U.S. Department of Energy, Office of Basic Energy Sciences, Division of Materials Sciences and Engineering under grant DE-SC0008772. X-ray scattering experiments were carried out at the Complex Materials Scattering (CMS) and the Soft Matter Interfaces (SMI) beamlines at the National Synchrotron Light Source II, which are U.S. DOE Office of Science Facilities at Brookhaven National Laboratory under contract no. DE-SC0012704. This research used resources of the Center for Functional Nanomaterials, supported by U.S. DOE Office of Science Facilities at Brookhaven National Laboratory under Contract No. DE-SC0012704. We would like to acknowledge the Imaging Facility of CUNY Advanced Science Research Center for the instrument use and technical assistance.

## REFERENCES

- (1) (a) Bae, W.-G.; Kim, H. N.; Kim, D.; Park, S.-H.; Jeong, H. E.; Suh, K.-Y. 25th Anniversary Article: Scalable Multiscale Patterned Structures Inspired by Nature: the Role of Hierarchy. *Adv. Mater.* **2014**, *26*, 675–700. (b) Prince, E.; Kumacheva, E. Design and applications of man-made biomimetic fibrillar hydrogels. *Nat. Rev. Mater.* **2019**, *4*, 99–115. (c) Grzelczak, M.; Vermant, J.; Furst, E. M.; Liz-Marzán, L. M. Directed Self-Assembly of Nanoparticles. *ACS Nano* **2010**, *4*, 3591–3605.
- (2) (a) Aida, T.; Meijer, E. W.; Stupp, S. I. Functional Supramolecular Polymers. *Science* **2012**, *335*, 813–817. (b) Su, Z.; Zhang, R.; Yan, X.-Y.; Guo, Q.-Y.; Huang, J.; Shan, W.; Liu, Y.; Liu, T.; Huang, M.; Cheng, S. Z. D. The role of architectural engineering in macromolecular self-assemblies via non-covalent interactions: A molecular LEGO approach. *Prog. Polym. Sci.* **2020**, *103*, 101230. (c) Barredo, D.; Lienhard, V.; de Léséleuc, S.; Lahaye, T.; Browaeys, A. Synthetic three-dimensional atomic structures assembled atom by atom. *Nature* **2018**, *561*, 79–82.
- (3) Chung, D. D. L. *Carbon Materials: Science and Applications*; World Scientific Publishing: Singapore, 2019.
- (4) (a) Jones, M. R.; Seeman, N. C.; Mirkin, C. A. Programmable materials and the nature of the DNA bond. *Science* **2015**, *347*, 1260901. (b) Macfarlane, R. J.; O'Brien, M. N.; Petrosko, S. H.; Mirkin, C. A. Nucleic Acid-Modified Nanostructures as Programmable Atom Equivalents: Forging a New "Table of Elements. *Angew. Chem., Int. Ed.* **2013**, *52*, 5688–5698. (c) Tian, Y.; Lhermitte, J. R.; Bai, L.; Vo, T.; Xin, H. L.; Li, H.; Li, R.; Fukuto, M.; Yager, K. G.; Kahn, J. S.; Xiong, Y.; Minevich, B.; Kumar, S. K.; Gang, O. Ordered

three-dimensional nanomaterials using DNA-prescribed and valence-controlled material voxels. *Nat. Mater.* **2020**, *19*, 789–796. (d) Vo, T.; Venkatasubramanian, V.; Kumar, S.; Srinivasan, B.; Pal, S.; Zhang, Y.; Gang, O. Stoichiometric control of DNA-grafted colloid self-assembly. *Proc. Natl. Acad. Sci. U. S. A.* **2015**, *112*, 4982–4987.

(5) (a) Wang, Y.; Wang, Y.; Breed, D. R.; Manoharan, V. N.; Feng, L.; Hollingsworth, A. D.; Weck, M.; Pine, D. J. Colloids with valence and specific directional bonding. *Nature* **2012**, *491*, 51–55. (b) Yao, G.; Li, J.; Li, Q.; Chen, X.; Liu, X.; Wang, F.; Qu, Z.; Ge, Z.; Narayanan, R. P.; Williams, D.; Pei, H.; Zuo, X.; Wang, L.; Yan, H.; Feringa, B. L.; Fan, C. Programming nanoparticle valence bonds with single-stranded DNA encoders. *Nat. Mater.* **2020**, *19*, 781–788. (c) Boles, M. A.; Talapin, D. V. Binary Assembly of PbS and Au Nanocrystals: Patchy PbS Surface Ligand Coverage Stabilizes the CuAu Superlattice. *ACS Nano* **2019**, *13*, 5375–5384. (d) Damasceno, P. F.; Engel, M.; Glotzer, S. C. Predictive Self-Assembly of Polyhedra into Complex Structures. *Science* **2012**, *337*, 453–457. (e) Feng, L.; Dreyfus, R.; Sha, R.; Seeman, N. C.; Chaikin, P. M. DNA Patchy Particles. *Adv. Mater.* **2013**, *25*, 2779–2783. (f) Travasset, A. Binary nanoparticle superlattices of soft-particle systems. *Proc. Natl. Acad. Sci. U. S. A.* **2015**, *112*, 9563. (g) Sun, S.; Yang, S.; Xin, H. L.; Nykpanchuk, D.; Liu, M.; Zhang, H.; Gang, O. Valence-programmable nanoparticle architectures. *Nat. Commun.* **2020**, *11*, 2279. (h) Travasset, A. Soft Skyrmions, Spontaneous Valence and Selection Rules in Nanoparticle Superlattices. *ACS Nano* **2017**, *11*, 5375–5382.

(6) (a) Trinh, T.; Liao, C.; Toader, V.; Barlog, M.; Bazzi, H. S.; Li, J.; Sleiman, H. F. DNA-imprinted polymer nanoparticles with monodispersity and prescribed DNA-strand patterns. *Nat. Chem.* **2018**, *10*, 184–192. (b) Choueiri, R. M.; Galati, E.; Thérien-Aubin, H.; Klinkova, A.; Larin, E. M.; Querejeta-Fernández, A.; Han, L.; Xin, H. L.; Gang, O.; Zhulina, E. B.; Rubinstein, M.; Kumacheva, E. Surface patterning of nanoparticles with polymer patches. *Nature* **2016**, *538*, 79–83. (c) Chen, G.; Gibson, K. J.; Liu, D.; Rees, H. C.; Lee, J.-H.; Xia, W.; Lin, R.; Xin, H. L.; Gang, O.; Weizmann, Y. Regioselective surface encoding of nanoparticles for programmable self-assembly. *Nat. Mater.* **2019**, *18*, 169–174. (d) Audus, D. J.; Starr, F. W.; Douglas, J. F. Valence, loop formation and universality in self-assembling patchy particles. *Soft Matter* **2018**, *14*, 1622–1630. (e) Chen, Q.; Bae, S. C.; Granick, S. Directed self-assembly of a colloidal kagome lattice. *Nature* **2011**, *469*, 381–384. (f) Xiong, Y.; Yang, S.; Tian, Y.; Michelson, A.; Xiang, S.; Xin, H.; Gang, O. Three-Dimensional Patterning of Nanoparticles by Molecular Stamping. *ACS Nano* **2020**, *14*, 6823–6833.

(7) (a) Huang, M.; Hsu, C.-H.; Wang, J.; Mei, S.; Dong, X.; Li, Y.; Li, M.; Liu, H.; Zhang, W.; Aida, T.; Zhang, W.-B.; Yue, K.; Cheng, S. Z. D. Selective assemblies of giant tetrahedra via precisely controlled positional interactions. *Science* **2015**, *348*, 424–428. (b) Edwardson, T. G.; Lau, K. L.; Bousmail, D.; Serpell, C. J.; Sleiman, H. F. Transfer of molecular recognition information from DNA nanostructures to gold nanoparticles. *Nat. Chem.* **2016**, *8*, 162–170. (c) Ben Zion, M. Y.; He, X.; Maass, C. C.; Sha, R.; Seeman, N. C.; Chaikin, P. M. Self-assembled three-dimensional chiral colloidal architecture. *Science* **2017**, *358*, 633. (d) Gröschel, A. H.; Walther, A.; Löbbling, T. I.; Schacher, F. H.; Schmalz, H.; Müller, A. H. E. Guided hierarchical co-assembly of soft patchy nanoparticles. *Nature* **2013**, *503*, 247–251.

(8) (a) Jacobs, W. M.; Reinhardt, A.; Frenkel, D. Rational design of self-assembly pathways for complex multicomponent structures. *Proc. Natl. Acad. Sci. U. S. A.* **2015**, *112*, 6313–6318. (b) Patra, N.; Tkachenko, A. V. Programmable self-assembly of diamond polymorphs from chromatic patchy particles. *Phys. Rev. E: Stat. Phys., Plasmas, Fluids, Relat. Interdiscip. Top.* **2018**, *98*, 032611. (c) Mahynski, N. A.; Mao, R.; Pretti, E.; Shen, V. K.; Mittal, J. Grand canonical inverse design of multicomponent colloidal crystals. *Soft Matter* **2020**, *16*, 3187–3194. (d) Pretti, E.; Zerze, H.; Song, M.; Ding, Y.; Mahynski, N. A.; Hatch, H. W.; Shen, V. K.; Mittal, J. Assembly of three-dimensional binary superlattices from multi-flavored particles. *Soft Matter* **2018**, *14*, 6303–6312.

(9) Seeman, N. C. DNA in a material world. *Nature* **2003**, *421*, 427–431.

- (10) Rothemund, P. W. K. Folding DNA to create nanoscale shapes and patterns. *Nature* **2006**, *440*, 297–302.
- (11) (a) Castro, C. E.; Kilchherr, F.; Kim, D.-N.; Shiao, E. L.; Wauer, T.; Wortmann, P.; Bathe, M.; Dietz, H. A primer to scaffolded DNA origami. *Nat. Methods* **2011**, *8*, 221–229. (b) Douglas, S. M.; Marblestone, A. H.; Teerapittayanon, S.; Vazquez, A.; Church, G. M.; Shih, W. M. Rapid prototyping of 3D DNA-origami shapes with caDNAno. *Nucleic Acids Res.* **2009**, *37*, 5001–6. (c) Douglas, S. M.; Dietz, H.; Liedl, T.; Hogberg, B.; Graf, F.; Shih, W. M. Self-assembly of DNA into nanoscale three-dimensional shapes. *Nature* **2009**, *459*, 414–448. (d) Dietz, H.; Douglas, S. M.; Shih, W. M. Folding DNA into Twisted and Curved Nanoscale Shapes. *Science* **2009**, *325*, 725–730. (e) Han, D.; Pal, S.; Nangreave, J.; Deng, Z.; Liu, Y.; Yan, H. DNA Origami with Complex Curvatures in Three-Dimensional Space. *Science* **2011**, *332*, 342–346. (f) Benson, E.; Mohammed, A.; Gardell, J.; Masich, S.; Czeizler, E.; Orponen, P.; Högberg, B. DNA rendering of polyhedral meshes at the nanoscale. *Nature* **2015**, *523*, 441–444. (g) Veneziano, R.; Ratanalert, S.; Zhang, K.; Zhang, F.; Yan, H.; Chiu, W.; Bathe, M. Designer nanoscale DNA assemblies programmed from the top down. *Science* **2016**, *352*, 1534. (h) Iinuma, R.; Ke, Y.; Jungmann, R.; Schlichthaerle, T.; Woehrstein, J. B.; Yin, P. Polyhedra self-assembled from DNA tripods and characterized with 3D DNA-PAINT. *Science* **2014**, *344*, 65–69.
- (12) (a) Schreiber, R.; Do, J.; Roller, E.-M.; Zhang, T.; Schüller, V. J.; Nickels, P. C.; Feldmann, J.; Liedl, T. Hierarchical assembly of metal nanoparticles, quantum dots and organic dyes using DNA origami scaffolds. *Nat. Nanotechnol.* **2014**, *9*, 74–78. (b) Urban, M. J.; Dutta, P. K.; Wang, P.; Duan, X.; Shen, X.; Ding, B.; Ke, Y.; Liu, N. Plasmonic Toroidal Metamolecules Assembled by DNA Origami. *J. Am. Chem. Soc.* **2016**, *138*, 5495–5498. (c) Lan, X.; Lu, X.; Shen, C.; Ke, Y.; Ni, W.; Wang, Q. Au Nanorod Helical Superstructures with Designed Chirality. *J. Am. Chem. Soc.* **2015**, *137*, 457–462.
- (13) (a) Maune, H. T.; Han, S.-p.; Barish, R. D.; Bockrath, M.; Goddard, W. A., III; Rothemund, P. W. K.; Winfree, E. Self-assembly of carbon nanotubes into two-dimensional geometries using DNA origami templates. *Nat. Nanotechnol.* **2010**, *5*, 61–66. (b) Pei, H.; Sha, R.; Wang, X.; Zheng, M.; Fan, C.; Canary, J. W.; Seeman, N. C. Organizing End-Site-Specific SWCNTs in Specific Loci Using DNA. *J. Am. Chem. Soc.* **2019**, *141*, 11923–11928. (c) Sun, W.; Shen, J.; Zhao, Z.; Arellano, N.; Rettner, C.; Tang, J.; Cao, T.; Zhou, Z.; Ta, T.; Streit, J. K.; Fagan, J. A.; Schaus, T.; Zheng, M.; Han, S.-J.; Shih, W. M.; Maune, H. T.; Yin, P. Precise pitch-scaling of carbon nanotube arrays within three-dimensional DNA nanotrenches. *Science* **2020**, *368*, 874.
- (14) (a) Ijäs, H.; Hakaste, I.; Shen, B.; Kostianen, M. A.; Linko, V. Reconfigurable DNA Origami Nanocapsule for pH-Controlled Encapsulation and Display of Cargo. *ACS Nano* **2019**, *13*, 5959–5967. (b) Zhao, Z.; Fu, J.; Dhakal, S.; Johnson-Buck, A.; Liu, M.; Zhang, T.; Woodbury, N. W.; Liu, Y.; Walter, N. G.; Yan, H. Nanocaged enzymes with enhanced catalytic activity and increased stability against protease digestion. *Nat. Commun.* **2016**, *7*, 10619.
- (15) (a) Jiang, Q.; Song, C.; Nangreave, J.; Liu, X.; Lin, L.; Qiu, D.; Wang, Z.-G.; Zou, G.; Liang, X.; Yan, H.; Ding, B. DNA Origami as a Carrier for Circumvention of Drug Resistance. *J. Am. Chem. Soc.* **2012**, *134*, 13396–13403. (b) Zhang, Q.; Jiang, Q.; Li, N.; Dai, L.; Liu, Q.; Song, L.; Wang, J.; Li, Y.; Tian, J.; Ding, B.; Du, Y. DNA Origami as an In Vivo Drug Delivery Vehicle for Cancer Therapy. *ACS Nano* **2014**, *8*, 6633–6643. (c) Zhao, Y.-X.; Shaw, A.; Zeng, X.; Benson, E.; Nyström, A. M.; Högberg, B. DNA Origami Delivery System for Cancer Therapy with Tunable Release Properties. *ACS Nano* **2012**, *6*, 8684–8691. (d) Wang, S.-T.; Gray, M. A.; Xuan, S.; Lin, Y.; Byrnes, J.; Nguyen, A. I.; Todorova, N.; Stevens, M. M.; Bertozzi, C. R.; Zuckermann, R. N.; Gang, O. DNA origami protection and molecular interfacing through engineered sequence-defined peptoids. *Proc. Natl. Acad. Sci. U. S. A.* **2020**, *117*, 6339.
- (16) Wang, P.; Meyer, T. A.; Pan, V.; Dutta, P. K.; Ke, Y. The Beauty and Utility of DNA Origami. *Chem.* **2017**, *2*, 359–382.
- (17) Hong, F.; Zhang, F.; Liu, Y.; Yan, H. DNA Origami: Scaffolds for Creating Higher Order Structures. *Chem. Rev.* **2017**, *117*, 12584–12640.
- (18) (a) Fu, Y.; Zeng, D.; Chao, J.; Jin, Y.; Zhang, Z.; Liu, H.; Li, D.; Ma, H.; Huang, Q.; Gothelf, K. V.; Fan, C. Single-Step Rapid Assembly of DNA Origami Nanostructures for Addressable Nanoscale Bioreactors. *J. Am. Chem. Soc.* **2013**, *135*, 696–702. (b) Woo, S.; Rothemund, P. W. K. Programmable molecular recognition based on the geometry of DNA nanostructures. *Nat. Chem.* **2011**, *3*, 620–627. (c) Zhang, F.; Jiang, S.; Wu, S.; Li, Y.; Mao, C.; Liu, Y.; Yan, H. Complex wireframe DNA origami nanostructures with multi-arm junction vertices. *Nat. Nanotechnol.* **2015**, *10*, 779–784. (d) Zhao, Z.; Liu, Y.; Yan, H. Organizing DNA Origami Tiles into Larger Structures Using Preformed Scaffold Frames. *Nano Lett.* **2011**, *11*, 2997–3002. (e) Aghebat Rafat, A.; Pirzer, T.; Scheible, M. B.; Kostina, A.; Simmel, F. C. Surface-Assisted Large-Scale Ordering of DNA Origami Tiles. *Angew. Chem., Int. Ed.* **2014**, *53*, 7665–7668. (f) Kocabay, S.; Kempter, S.; List, J.; Xing, Y.; Bae, W.; Schiffls, D.; Shih, W. M.; Simmel, F. C.; Liedl, T. Membrane-Assisted Growth of DNA Origami Nanostructure Arrays. *ACS Nano* **2015**, *9*, 3530–3539. (g) Suzuki, Y.; Endo, M.; Sugiyama, H. Lipid-bilayer-assisted two-dimensional self-assembly of DNA origami nanostructures. *Nat. Commun.* **2015**, *6*, 8052. (h) Zhang, T.; Hartl, C.; Frank, K.; Heuer-Jungemann, A.; Fischer, S.; Nickels, P. C.; Nickel, B.; Liedl, T. 3D DNA Origami Crystals. *Adv. Mater.* **2018**, *30*, 1800273. (i) Wagenbauer, K. F.; Sigl, C.; Dietz, H. Gigadalton-scale shape-programmable DNA assemblies. *Nature* **2017**, *552*, 78–83. (j) Mohammed, A. M.; Šulc, P.; Zenk, J.; Schulman, R. Self-assembling DNA nanotubes to connect molecular landmarks. *Nat. Nanotechnol.* **2017**, *12*, 312–316.
- (19) (a) Li, Z.; Liu, M.; Wang, L.; Nangreave, J.; Yan, H.; Liu, Y. Molecular Behavior of DNA Origami in Higher-Order Self-Assembly. *J. Am. Chem. Soc.* **2010**, *132*, 13545–13552. (b) Bayrak, T.; Helmi, S.; Ye, J.; Kauert, D.; Kelling, J.; Schönherr, T.; Weichelt, R.; Erbe, A.; Seidel, R. DNA-Mold Templated Assembly of Conductive Gold Nanowires. *Nano Lett.* **2018**, *18*, 2116–2123. (c) Buchberger, A.; Simmons, C. R.; Fahmi, N. E.; Freeman, R.; Stephanopoulos, N. Hierarchical Assembly of Nucleic Acid/Coiled-Coil Peptide Nanostructures. *J. Am. Chem. Soc.* **2020**, *142*, 1406–1416.
- (20) (a) Liu, W.; Zhong, H.; Wang, R.; Seeman, N. C. Crystalline two-dimensional DNA-origami arrays. *Angew. Chem., Int. Ed.* **2011**, *50*, 264–267. (b) Tikhomirov, G.; Petersen, P.; Qian, L. Programmable disorder in random DNA tilings. *Nat. Nanotechnol.* **2017**, *12*, 251–259. (c) Tikhomirov, G.; Petersen, P.; Qian, L. Fractal assembly of micrometre-scale DNA origami arrays with arbitrary patterns. *Nature* **2017**, *552*, 67–71. (d) Wang, P.; Gaitanaros, S.; Lee, S.; Bathe, M.; Shih, W. M.; Ke, Y. Programming Self-Assembly of DNA Origami Honeycomb Two-Dimensional Lattices and Plasmonic Metamaterials. *J. Am. Chem. Soc.* **2016**, *138*, 7733–7740. (e) Liu, W. Y.; Halverson, J.; Tian, Y.; Tkachenko, A. V.; Gang, O. Self-organized architectures from assorted DNA-framed nanoparticles. *Nat. Chem.* **2016**, *8*, 867–873.
- (21) (a) Tian, Y.; Zhang, Y. G.; Wang, T.; Xin, H. L. L.; Li, H. L.; Gang, O. Lattice engineering through nanoparticle-DNA frameworks. *Nat. Mater.* **2016**, *15*, 654–661. (b) Liu, W. Y.; Tagawa, M.; Xin, H. L. L.; Wang, T.; Emamy, H.; Li, H. L.; Yager, K. G.; Starr, F. W.; Tkachenko, A. V.; Gang, O. Diamond family of nanoparticle superlattices. *Science* **2016**, *351*, 582–586.
- (22) Liu, K.; Nie, Z.; Zhao, N.; Li, W.; Rubinstein, M.; Kumacheva, E. Step-Growth Polymerization of Inorganic Nanoparticles. *Science* **2010**, *329*, 197.
- (23) Kuzyk, A.; Schreiber, R.; Fan, Z.; Pardatscher, G.; Roller, E.-M.; Högele, A.; Simmel, F. C.; Govorov, A. O.; Liedl, T. DNA-based self-assembly of chiral plasmonic nanostructures with tailored optical response. *Nature* **2012**, *483*, 311–314.
- (24) (a) Anderson, J. A.; Glaser, J.; Glotzer, S. C. HOOMD-blue: A Python package for high-performance molecular dynamics and hard particle Monte Carlo simulations. *Comput. Mater. Sci.* **2020**, *173*, 109363. (b) Anderson, J. A.; Eric Irrgang, M.; Glotzer, S. C. Scalable

Metropolis Monte Carlo for simulation of hard shapes. *Comput. Phys. Commun.* **2016**, *204*, 21–30.

(25) (a) Zha, X.; Travasset, A. Stability and Free Energy of Nanocrystal Chains and Superlattices. *J. Phys. Chem. C* **2018**, *122*, 23153–23164. (b) Padovan-Merhar, O.; Lara, F. V.; Starr, F. W. Stability of DNA-linked nanoparticle crystals: Effect of number of strands, core size, and rigidity of strand attachment. *J. Chem. Phys.* **2011**, *134*, 244701. (c) Pretti, E.; Mao, R.; Mittal, J. Modelling and simulation of DNA-mediated self-assembly for superlattice design. *Mol. Simul.* **2019**, *45*, 1203–1210.